Applied Catalysis B: Environmental 130–131 (2013) 54–64

Contents lists available at SciVerse ScienceDirect

Applied Catalysis B: Environmental

journal homepage: www.elsevier.com/locate/apcatb

NO_x storage capacity of yttria-stabilized zirconia-based catalysts

W.Y. Hernández [a], A. Hadjar [a], M. Klotz [b], J. Leloup [b], A. Princivalle [b], C. Tardivat [b], C. Guizard [b], P. Vernoux [a,*]

[a] Université Lyon 1, CNRS, UMR 5256, IRCELYON, Institut de Recherches sur la Catalyse et l'Environnement de Lyon, 2 Avenue Albert Einstein, F-69626 Villeurbanne, France
[b] Laboratoire de Synthèse et Fonctionnalisation des Céramiques, UMR3080, CNRS/Saint-Gobain CREE – 550, Av. Alphonse Jauffret – 84306 Cavaillon Cedex, France

ARTICLE INFO

Article history:
Received 25 July 2012
Received in revised form
19 September 2012
Accepted 26 September 2012
Available online 22 October 2012

Keywords:
Yttria-stabilized zirconia
Oxygen vacancies
Ionic conductor
NO_x storage-reduction
Diesel particulate filters

ABSTRACT

A NO*x* chemisorption study was performed on yttria-stabilized zirconia (YSZ), an O^{2-} ionically conducting ceramic. NO_2 chemisorption on YSZ as well as $NO + O_2$ interactions on Pt/YSZ catalyst were clearly correlated to the presence of surface oxygen vacancies. A remarkable NO*x* storage capacity was obtained on Pt/YSZ powdered catalysts, by combining nitrates formation and NO_2 adsorption on oxygen vacancies. Under cycling conditions (lean phase/rich phase: 3 min/2 min) and using propene as a reductant, powdered Pt-Rh catalyst exhibited overall NO*x* abatement conversion of around 75% at 250 and 300 °C. Pt/Rh/YSZ catalysts were finely dispersed in the porosity of SiC mini diesel particulate filters (DPFs). Quite reproducible and stable NO*x* conversions were achieved in cycling conditions with values around 50% between 250 and 400 °C. In addition, YSZ-based catalysts have shown high thermal resistance and sulfur tolerance.

1. Introduction

Nitrogen oxides (NO and NO_2) are among the most frequent and harmful atmospheric pollutants, because they have many-fold devastating effects on the atmosphere and ecosystems (such as ozone layer depletion and acid rain) as well as on human health. Considering that the NO*x* production from mobile sources almost contributes half of the overall NO*x* emission, many countries such as those belonging to European Community and U.S. have defined stringent standards in NO*x* concentrations emitted by automotives. Efficient catalytic post-treatment (three-way converter) is now commonly implemented in gasoline cars while the issue is more challenging for diesel vehicles which are working in lean-burn conditions. However, the future EURO 6 legislation, from 2014, will require extremely low emission levels of NO*x* decreasing from 0.18 g/km (actual EURO 5 standard) down to 0.08 g/km. The challenge addressed to the scientific catalysis community is to find smart catalysts able to selectively reduce NO*x* into environmentally benign N_2 in a gaseous environment containing high excesses of oxygen and trace amounts of reducing agents (un-burnt hydrocarbons and carbon monoxide). In this context, NO*x* storage-reduction (NSR) catalytic technology emerges as a promising solution for removal of NO*x* from these engines [1]. NSR catalysts work in cyclic gas-composition conditions. During the first step (lean phase), NSR materials store emitted NO*x* as nitrates until the surface reaches the saturation threshold. A pulse of fuel post-injection then triggers the short second step (rich phase), during which the reducing conditions lead to nitrate decomposition and release as well as subsequent NO*x* reduction into N_2 and surface regeneration. NSR catalysts have been strongly developed and improved during the last fifteen years [2,3]. These kinds of materials are commonly composed of Pt nanoparticles to activate NO oxidation into NO_2 in the lean phase, a storage basic compound (typically K or Ba) to form nitrates from NO_2, Rh nanoparticles to reduce NO*x* into N_2 in the rich phase and an oxide support. The NSR technology is in competition with the selective catalytic reduction of NO*x* by urea (urea-SCR) which can be efficiently implemented using noble-metal free catalysts [3]. Even if the urea-SCR requires an additional tank of urea and a controlled injection and decomposition of urea, this technology is now commonly developed for heavy-duty vehicles. However, NSR catalysts can be inserted into the porosity of diesel particulate filters (DPFs), thus strongly decreasing the required space of the after-treatment. This DPNR technology, for diesel particulate – NO*x* reduction, initiated by the Toyota group [4] combines soot and NO*x* abatement. Therefore, this solution seems to be particularly suitable for compact cars [5]. NSR and DPNR catalysts must be sulfur and temperature resistant and must contain low noble metal loadings to compete with the urea-SCR technology. In addition, the fuel overconsumption provoked by the fuel post-injection during the rich phases must absolutely be minimized in order to achieve European Community CO_2 exhaust emission standards which were fixed at 95 g of CO_2 per km from 2020. This limit value affects all

* Corresponding author. Tel.: +33 4 72431587; fax: +33 4 72431695.
E-mail address: philippe.vernoux@ircelyon.univ-lyon1.fr (P. Vernoux).

0926-3373/$ – see front matter © 2012 Elsevier B.V. All rights reserved.
http://dx.doi.org/10.1016/j.apcatb.2012.09.048

car manufacturers and is calculated from the CO_2 emissions average of their fleet. DPNR catalysts, impregnated inside the porosity of DPFs, must also be compatible with regeneration steps of the DPFs which are triggered by fuel post-injections, and which provoke hot points due to fast soot particles oxidation. Temperatures as high as 750–800 °C can be reached in the DPF inlet channels [6,7]. A synergetic effect between post-injections and catalytic activity of the DPNR catalyst toward soot oxidation is expected to promote DPFs regeneration and thus decrease both the quantity of post-injected fuel and the minimal temperature for soot ignition.

Recently, we have shown [8] that the NO*x* storage capacity of an electrochemical Pt-Ba/YSZ (yttria-stabilized zirconia, an ionically conducting ceramic) catalyst can be strongly promoted by cathodic polarizations, even under lean-burn conditions. Electrochemical activation of the NO*x* storage capacity was linked with the ionic conductivity of YSZ and the presence of oxygen vacancies on the YSZ surface, which can act as NO_2 adsorption sites. In addition, YSZ is able to burn soot particulates without the use of noble metal [9]. The aim of this paper is to use YSZ as an alternative support for the DPNR technology. The targeted application is to implement NSR catalysts into the DPFs to perform concomitant soot and NO*x* removal and to decrease the catalyst volume. Yttria-stabilised zirconia is compatible with high temperatures that can occur during DPF regeneration phases, as it exhibits a cubic structure which is well-known to be temperature-resistant. The present work focuses on the NO*x* storage capacity of YSZ-based systems. The NO*x* storage capacity of the bare-YSZ support and Pt/YSZ catalysts was measured at 250 °C. The NSR cycling experiments were carried out between 200 and 300 °C on Pt/Rh/YSZ catalysts in form of powders or deposited in the porosity of silicon carbide mini-DPFs. Finally, aging tests were performed at high temperatures and in presence of SO_2.

2. Experimental

2.1. Catalyst preparation

2.1.1. Preparation of the powdered catalysts

Platinum and rhodium nanoparticles were dispersed over 8 mol% yttria-stabilized zirconia (8YSZ, $(ZrO_2)_{0.92}(Y_2O_3)_{0.08}$) supplied by TOSOH®. The platinum and rhodium precursors were diammineplatinum(II) nitrite, $(NH_3)_2Pt(NO_2)_2$ (Alfa Aesar, 1.7 wt.% of Pt) and $Rh(NO_3)_3$ (Alfa-Aesar, 10 wt.% of Rh). The catalysts were prepared by incipient wet impregnation method. The impregnation was performed at 70 °C for 70 min under stirring at atmospheric pressure. Then, the excess water was eliminated at 40 °C under vacuum and the remaining powder was dried at 110 °C overnight. Finally, the catalysts were annealed at 500 °C for 1 h in air flow, and then reduced under flowing 100% H_2 at 500 °C for 1 h. The powdered Pt/YSZ/Rh catalyst was prepared in two successive steps. The first step was Pt impregnation, followed by drying at 40 °C and calcination at 500 °C for 1 h. Then, Rh impregnation was performed, followed by the same drying and calcination procedures. The target Pt and Rh loading in both Pt/YSZ and Pt-Rh/YSZ powdered catalysts was 0.5 wt.%.

2.1.2. Preparation of the DPF-catalysts

Pt/Rh/YSZ catalysts were deposited in the porosity of SiC mini-DPFs produced by SAINT-GOBAIN. These small non-plugged DPFs (Fig. 1) have the following characteristics: cell density = 181 cpsi, diameter = 25 mm, length = 50 mm; pore diameter of channel walls = 15 μm, porosity of channel walls = 47%, and thickness of channel walls = 370 μm. The deposition of Pt/Rh/YSZ catalysts onto the SiC-DPFs was performed in three successive steps. A suspension containing a low loading (<3 wt.%) of 8YSZ ($(ZrO_2)_{0.92}(Y_2O_3)_{0.08}$, TOSOH®) was initially prepared in a mixture of water and ethanol (40 vol.% of H_2O). The dispersion was accomplished by 15 min vibration in an ultrasonic bath. Concentration of the suspension was around 20 g/l. The supports were dipped in this suspension which can penetrate by capillarity into the channels and the wall porosity of SiC-DPFs. After a few minutes, the suspension was clear, showing that YSZ was filtered by the DPF. The substrate was then dried at 40 °C and calcined at 550 °C for 1 h. The YSZ loading was around 90 g/l of DPF. The next step involved a second immersion of the SiC mini-DPF in a solution based on water and ethanol (40 vol.% of H_2O) of Pt precursor ($(NH_3)_2Pt(NO_2)_2$, Alfa Aesar, 1.7 wt.% of Pt) in order to disperse Pt nanoparticles onto the YSZ layer. After drying at 40 °C and calcining at 500 °C for 1 h, the same procedure was repeated in an aqueous solution of Rh precursor ($(Rh(NO_3)_3$, Alfa-Aesar, 10 wt.% of Rh) to disperse Rh nanoparticles on the porous washcoat. Finally, the SiC-DPF substrate was dried at 40 °C and calcined in air at 500 °C for 1 h. Deposition of Pt particles and deposition of Rh particles were not performed simultaneously in order to minimize interparticle interactions. The target of overall PGM loading was 1 wt.% with a ratio Pt/Rh = 2.

2.2. Catalysts characterizations

The Pt and Rh loadings in powdered catalysts were measured by inductively coupled plasma-emission spectroscopy, ICP-OES (Varian). The specific surface area (SSA) was determined by the BET method (Quantachrom, Mod. Nova 2000), using nitrogen adsorption at −195 °C. The catalysts were observed by HRTEM (High-resolution transmission electronic microscopy, JEOL 2010 LaB6) for investigating the morphology and size of Pt and Rh particles. Metallic dispersions were measured by using H_2-pulse chemisorption technique with an AutoChemII 2920 station from Micromeritics using the procedure developed for YSZ support [10]. The samples (200 mg), placed in a U-shaped quartz reactor with an inner diameter of 0.5 cm, were pretreated under 40% H_2 in He at 500 °C for 2 h. Then, catalysts were cooled down, under an argon flow of 50 mL/min, to −28 °C (temperature of the pulse-chemisorption). Pulses of H_2 (3% H_2 in Ar, AIR LIQUID, 99.99% purity) were injected in the catalytic reactor corresponding to 0.47 μmol of H_2. Hydrogen consumptions were measured with a TCD. The signals were monitored by a computer and data were analyzed using Origin software.

The loadings of Pt and Rh into the SiC-DPF were determined by measuring the metallic concentration (by ICP-OES, inductively coupled plasma-emission spectroscopy, VARIAN) of the precursor solutions before and after deposition.

2.3. NOx storage capacity measurements

NO*x* adsorption measurements were carried out using a conventional fixed bed quartz reactor under atmospheric pressure and isothermal temperature (250 °C). Two different inlet gas mixtures were employed (flow rate: 10 L h^{-1}), depending of the tested materials: 500 ppm NO_2 in He for YSZ (no NO oxidation takes place on this material formulation) or 500 ppm NO, 6.5% O_2 and He as balance for the Pt/YSZ solid.

The sample (300 mg) was first pretreated in 10% O_2 in He by heating from room temperature to 600 °C and holding at 600 °C for 1 h, and then cooled down to 250 °C. At this temperature, the sample was cleaned by flow of He (10 L h^{-1}) during 30 min. The adsorption measurement was carried out by exposing the solid to the adequate gas mixture until the adsorption amount of NO*x* reached its saturation capacity. Thereafter, the sample was heated from 250 °C to 600 °C at a constant temperature rate of 10 °C min^{-1} in a stream of He, at a total flow rate of 10 L h^{-1}. The desorbed gas effluent

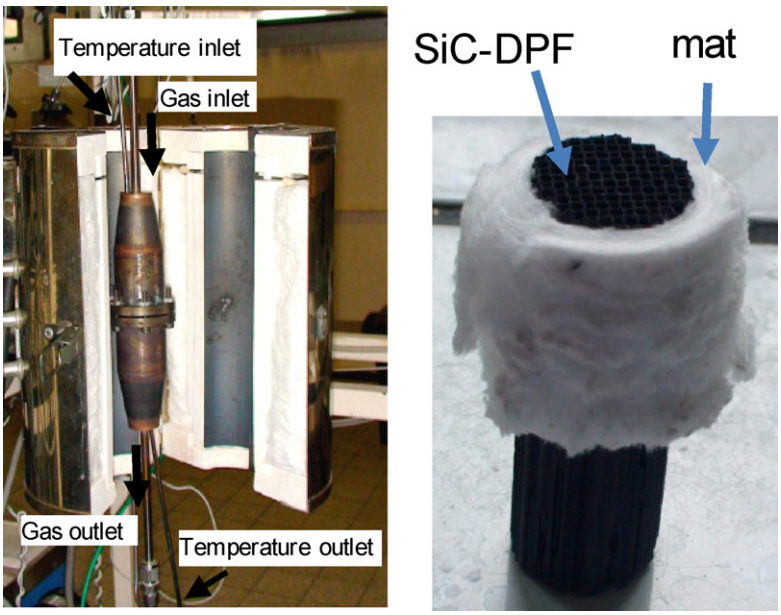

Fig. 1. Photos of the steel bi-compartment reactor (left) and of a DPF sample wrapped in a vermiculite-coated fiber mat (right).

of NO and NO_2 was continuously recorded by an on-line analyzer EMERSON NGA2000.

2.4. Catalytic performances measurements

2.4.1. NOx storage reduction (NSR) on powdered Pt-Rh/YSZ catalyst

The NSR cyclic measurements were performed in a conventional U-shaped fixed bed quartz reactor (i.d. = 8 mm), under atmospheric pressure at the desired reaction temperature (200, 250 or 300 °C) with 200 mg of catalyst. The gas hourly space velocity (GHSV) was around 100,000 h^{-1}. Prior to each experiment, the sample was pretreated in 10% O_2 in He at 600 °C for 1 h. The reactor was connected to a four-way valve, which provides quick switching between lean and rich atmospheres. Constant flows (10 L h^{-1}) of lean reactive mix (500 ppm NO*x*/500 ppm C_3H_6/6.5% O_2/10% H_2O and He as balance) or rich reactive mix (500 ppm NO*x*/500 ppm C_3H_6 and He as balance) were alternated through periods of 3 min and 2 min, respectively. The catalyst was exposed to 12 consecutive lean/rich cycles.

Reactants and products analysis was performed using an on-line gas micro-chromatograph (Varian CP2003 equipped with two TCD detectors, a molecular sieve and a Porapak Q column for CO, N_2O, C_3H_8, CH_4, C_3H_6, CO_2 and H_2 analysis) and IR and UV on-line analyzers (EMERSON NGA2000 for CO, CO_2, NO, NO_2 and N_2O analysis). Reactants were LINDE certified standards of NO in He (1990 ppm), C_3H_6 in He (8005 ppm), O_2 (99.999%) which could be further diluted in (99.999%) He. H_2O vapor was introduced using an atmospheric pressure Pyrex saturator thermostated at 43.6 °C, which produced a vapor pressure of 1013 Pa.

The NO*x* conversion for a complete representative cycle was calculated according to the following formula:

$$\%NO_x \text{ conversion} = \frac{(NO_{x,in} - NO_{x,out})}{NO_{x,in}} \times 100 \quad (1)$$

The global NO*x* conversion into N_2 (selectivity of the process) was estimated considering the production of N_2O during a complete cycle:

$$\%\,NO_x \text{ conversion into } N_2 = \frac{(NO_{x,in} - NO_{x,out} - 2N_2O_{out})}{NO_{x,in}} \times 100 \quad (2)$$

Carbon and nitrogen mass balances were found to be within 2%. NO*x* conversions reported in the manuscript correspond to stable and reproducible values, i.e. after several lean/rich cycles and for 3 identical Pt-Rh/DPF samples.

2.4.2. NOx storage reduction on Pt-Rh/DPF

Catalytic performances for NO*x* removal of Pt-Rh/YSZ catalysts deposited in SiC-DPFs were evaluated by using a steel bi-compartment reactor (Fig. 1). Gas-tightness was ensured by a mica seal located between the two compartments. The inlet and outlet of the reactor were cone-shaped in order to homogenize the gas distribution across the DPFs. Before being placed in the reactor, DPFs were wrapped in a vermiculite-coated fiber mat which provided insulation and prevented gas slippage around the monolith. Two thermocouples were located at the entrance and the exit of the mini-DPF. We did not observe significant temperature differences during lean/rich cycles in diesel exhaust conditions. Before catalytic performance measurements, Pt-Rh/DPF samples were pretreated at 500 °C in O_2 (10 vol.% in He) for 12 h to stabilize the catalyst morphology and allow the expansion of the fiber mat. The NO*x* storage-reduction activity of Pt-Rh/DPFs was investigated at 200 °C, 250 °C and 300 °C under alternative rich and lean atmospheres. The lean phase (1 min) was composed of $NO/C_3H_6/O_2/H_2O$: 500 ppm/500 ppm/6.5 vol%/10 vol% while the rich phase (30 s) contained NO/C_3H_6 = 500 ppm/500 ppm. The overall flow was 40 L h^{-1} which corresponded to a space velocity of 1700 h^{-1}. The catalytic performance was investigated along 10 successive lean/rich cycles and repeated 3 times for each composition. Product analysis and calculations were performed in the same way as already described in Section 2.4.1.

3. Results and discussions

3.1. Catalysts characterizations

The chemical composition and surface area of the synthesized catalysts are summarized in Table 1. Pt and Rh loadings in the prepared materials are approximately the same as the target value indicating no appreciable loss of metal during the deposition procedure. In addition, the presence of the noble metals does not seem

Table 1
List and mains properties of catalysts.

Catalysts	Formulation	S_{BET} ($m^2\ g^{-1}$)	wt.%	
			Pt	Rh
Pt	Pt/YSZ	13.8	0.35	–
Pt-Rh	Pt/YSZ/Rh	13.5	0.46	0.48
Pt-Rh/DPF	Pt/YSZ/Rh//SiC-DPF	32	0.67	0.33

Table 2
Results of NO*x* adsorption–desorption processes on YSZ and Pt/YSZ.

Solid	Adsorption process ($\mu mol/g_{cat}$)		Desorption process ($\mu mol/g_{cat}$)	
	NO*x* stored	NO produced	NO_2	NO
YSZ	46	23	44	4
Pt/YSZ	34	–	13	18

to affect the surface area of the bare YSZ support (~13 $m^2\ g^{-1}$). In the case of the Pt-Rh/DPF material, the relevant increase in S_{BET} value in comparison to Pt-Rh one can be associated to the porous structure of the SiC substrate.

The morphology and microstructure of the synthesized catalysts were analyzed by TEM and SEM techniques. Fig. 2 shows representative TEM images of the Pt and Pt-Rh powdered materials. It is observed that the active phase in Pt/YSZ solid is fairly well dispersed with a particle size distribution from 4 to 15 nm (Fig. 2a), centered above 8 nm. On Pt-Rh/YSZ catalyst (Fig. 2b), both Pt and Rh nanoparticles show good dispersion and homogeneous particle size. In this catalyst, the particle size of Pt remains similar to that observed on Pt/YSZ solid, while the average particle size of Rh is considerably smaller (around 2–5 nm). The Pt-Rh/DPF sample was also studied by TEM microscopy by using the replica technique [11]. A representative image of this material is presented in Fig. 3. As can be observed, the Pt and Rh particle sizes are significantly smaller than that observed in Pt-Rh catalyst. The corresponding histogram reveals that the particle size distribution is very narrow and nearly monodispersed around 2 nm. It was possible to distinguish Pt from Rh nanoparticles by using EDX analysis which gave a Rh/Pt elemental ratio of 0.30, close to that observed by ICP (0.49). Thus, the improved metallic dispersion on Pt-Rh/DPF catalyst in comparison to Pt-Rh powdered material seems to indicate that phenomena occurring during impregnation of monolithic structures do not differ fundamentally from those occurring on conventional supported catalysts [12]. Several literature works have been focused in the influence of the parameters involved in the preparation of monolithic catalyst [12–14]. In general, the impregnation and drying methodologies became key factors in order to obtain monoliths with a uniform active phase distribution and it can be related to the capillary effects involved in these steps. In the present study, the evaluation of the synthesis conditions employed to obtain the Pt-Rh/SiC monolithic structure does not constitute the central aim of the work. Nevertheless, additional experiments start to be addressed to further investigate these interesting results.

The location of the catalyst in the SiC-monolithic structure was also studied by SEM technique (Fig. 4). The global SEM image of a cross-section between 4 channels as well as X-ray mappings of Zr and Si elements (Fig. 4b) of a DPF porous wall clearly show that the YSZ washcoat does not affect the porous structure of the DPFs and homogeneously covers the surface of the SiC grains both in the channels and inside the walls. More details can be observed in Fig. 5, where the SEM images of the unfilled-resin sample shows that the YSZ catalyst does not block any pores of the DPF wall structure (Fig. 5a). In addition, the deposited YSZ layer is mainly composed of small (~200 nm) and well distributed particles on the SiC grains. The particle size observed in this YSZ layer is very close to the crystal domain size calculated for such material from the XRD pattern, using the Scherrer equation (data not shown here).

3.2. NOx adsorption

3.2.1. NO_2 storage capacity of YSZ

The NO*x* storage capacity of YSZ was investigated at 250 °C, which is a typical value of diesel exhaust gas temperature in a DPF. NO_2 was adsorbed on the YSZ surface. We have checked that since this material exhibits no catalytic activity for NO oxidation into NO_2 under lean-burn conditions below 400 °C. Fig. 6a depicts the evolution of NO_2 and NO concentrations in the outlet stream during exposure of YSZ powder to NO_2. Note here that the NO concentration impurity in the NO_2 inlet gas is lower than 10 ppm. During the first seconds, the NO_2 concentration rapidly decays and reaches a minimum value above 200 ppm after 47 s. Then, the NO_2 concentration quickly increases while the NO production starts (~120 s after NO_2 injection), reaching a maximum concentration above 100 ppm and finally gradually decreases with time to become negligible after 30 min. During this NO production, no oxygen desorption is detected in the gas phase. After 30 min of NO_2 exposure, both NO_2 and NO profiles tend to their respective inlet values. This means that the saturation of the YSZ-adsorption capacity is reached. No relevant evolution of N_2O species is observed during this process. This result indicates that a significant amount of NO_2 is reduced into NO; NO production reaches a maximum after 330 s. The nitrogen balance, determined from the NO_2 consumption and the NO emission, shows that only part of the total consumed NO_2 (69 $\mu mol/g_{cat}$) is reduced into NO (23 $\mu mol/g_{cat}$) and consequently an important part of NO_2 is also stored on the YSZ surface (46 $\mu mol/g_{cat}$). NO_2 storage could occur via NO_2 disproportionation as observed on $Pt/Ba/Al_2O_3$ NSR catalyst [15–17]. This storage process consists of NO_2 adsorption on Ba followed by nitrate formation with concomitant production of NO. The NO_2 disproportionation implies that the oxidation of a NO_2 molecule to nitrate species takes place with the participation of another NO_2 molecule. The NO production on YSZ approximately corresponds to 33% of the total NO_2 adsorbed which is in good agreement with the disproportionation mechanism. The adsorption of NO_2 probably takes place on the YSZ surface oxygen vacancies as already reported in the literature with defective oxide surface [8,18–20]. For instance, Daturi et al. [20] have clearly evidenced the correlation between the deNO*x* activity of CeO_2 and the amount of oxygen vacancies present on the surface. In addition, by using dense YSZ membrane, we have recently linked [8] the NSC of Pt-Ba/YSZ electrochemical catalyst with the oxygen vacancy surface concentration induced under cathodic polarizations. However, Liu et al. [19] have investigated the NO_2 interactions with cubic YSZ at 300 K and concluded that NO_2 is the predominant stored species with concomitant oxidation of Zr^0 and Zr^{2+} ions. These authors suggested that the existence of oxygen vacancies prevents the formation of nitrate species.

To evaluate the nature of the adsorbed species, a TPD analysis under He was performed after NO_2 adsorption (Fig. 6b). The main feature is an intense peak of NO_2, centered at 420 °C, which confirms that a significant part of NO_2 (44 $\mu mol/g_{cat}$) was stored on the YSZ surface during the adsorption step (Table 2). The TPD spectrum also shows a comparatively small desorption peak of NO (4 $\mu mol/g_{cat}$), centered at above 495 °C, which corresponds to the NO/NO_2 thermodynamic equilibrium. This release of NO and NO_2 can be associated to the formation and stabilization of zirconium nitrates, nitrites and/or zirconium oxy-nitrates $[ZrO(NO_3)_2]$ on the weak Zr^{4+} basic sites of the YSZ surface [21–23] via NO_2 disproportionation initiated by NO_2 chemisorption on the surface oxygen vacancies. The overall amount of NO*x* release during desorption can be estimated to 48 $\mu moles/g_{cat}$,

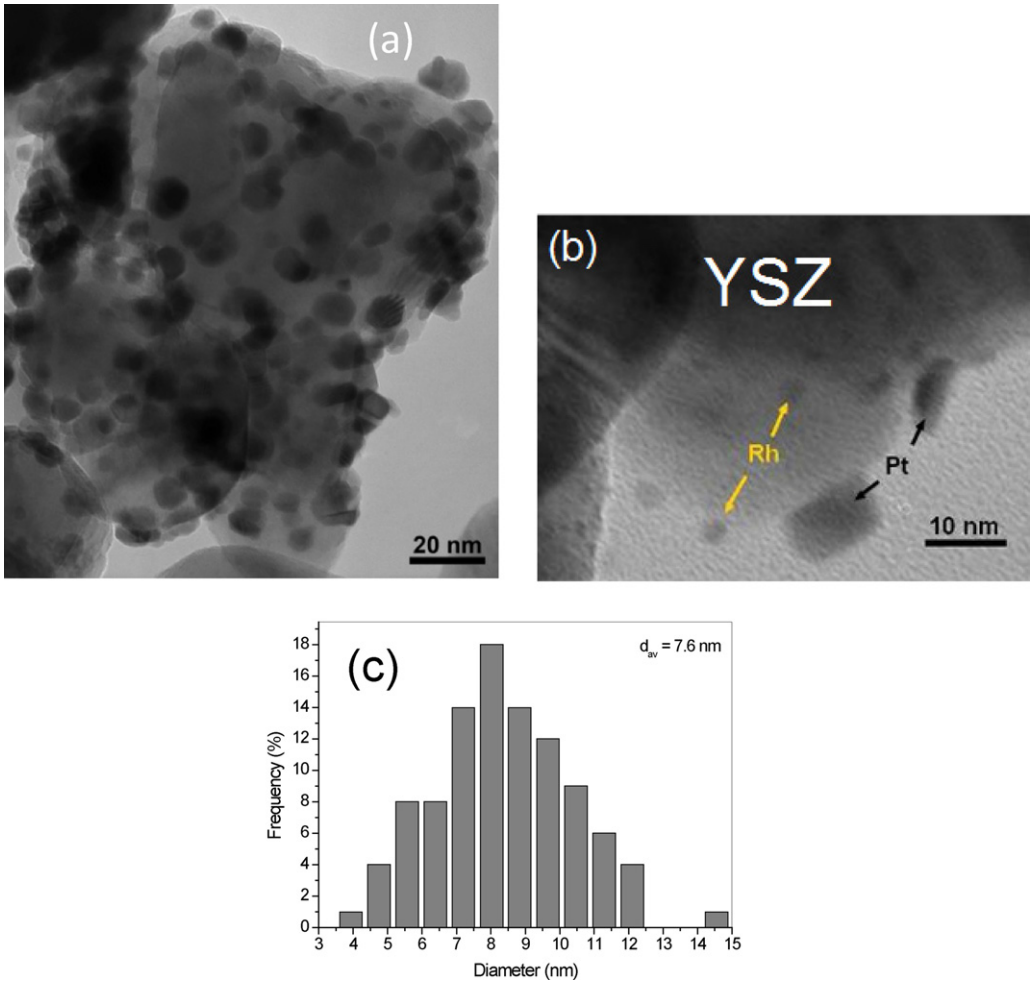

Fig. 2. TEM images of Pt (a) and Pt-Rh (b) powdered catalysts. Pt nanoparticles size distribution in Pt/YSZ catalyst (c).

in very good agreement with the NO_2 storage (46 μmol/g_{cat}) calculated during the adsorption step. These results also demonstrate that in the absence of oxygen, NO_2 storage mainly occurs via surface oxygen vacancies, i.e. around 44 μmol/g_{cat}. Indeed, several studies in the literature [24–26] have investigated the surface oxygen vacancies concentration on YSZ and found values between 4.7 and 5 μmol/m^2, i.e. 60 μmol/g_{cat}. This value is in good agreement with the quantity of NO_2 adsorbed or reduced into NO on surface oxygen vacancies on our sample, i.e. 69 μmoles/g_{cat}.

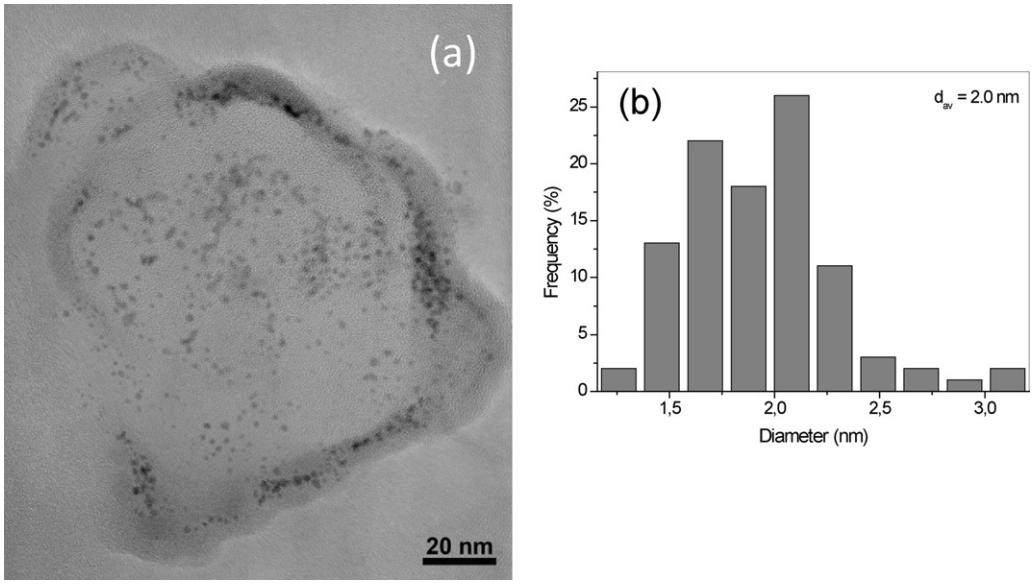

Fig. 3. TEM image of Pt-Rh/SiC powder (a) and the size statistic distribution of metallic nanoparticles (b).

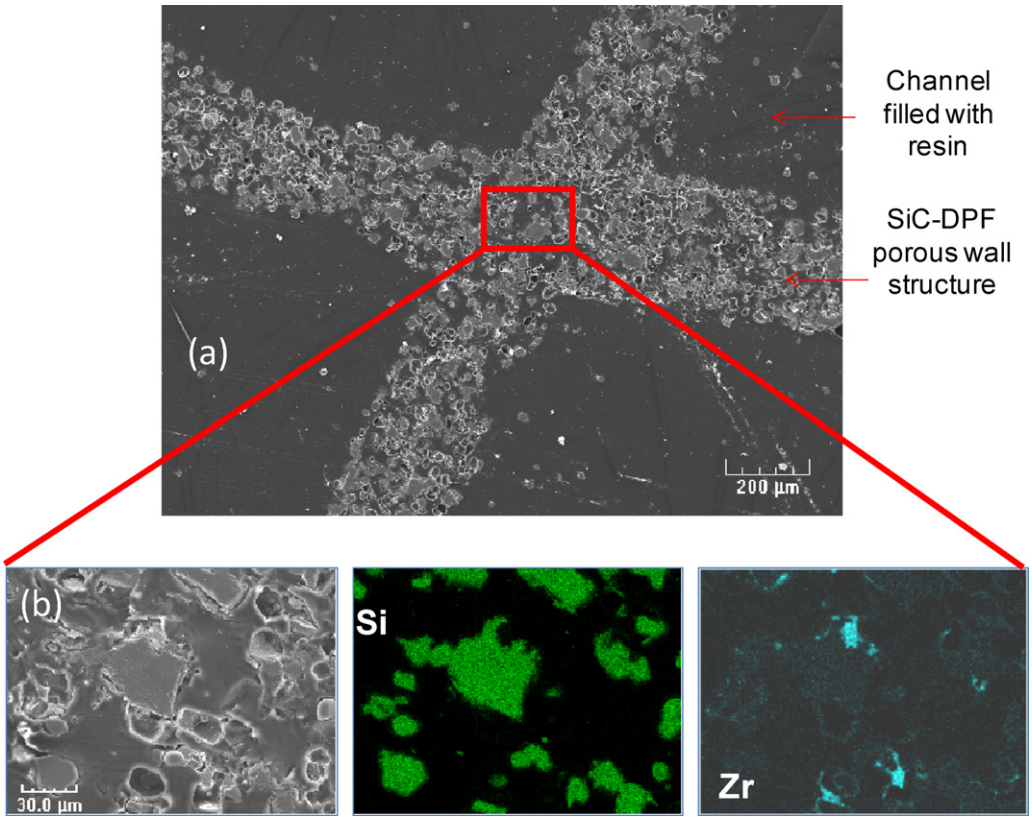

Fig. 4. SEM micrograph of a cross-section of the Pt-Rh/DPF (4 channels) (a) and SEM micrograph of a porous wall with associated EDX mapping of Si and Zr elements (b).

These experiments indicate that the interaction of NO_2 on YSZ surface takes place in 2 steps. The first one corresponds to NO_2 adsorption on oxygen vacancies which is predominant during at least 2 min before NO production. The second phase starts 2 min after NO_2 introduction and could be associated with the disproportionation of NO_2 molecules which produce NO release and nitrates formation. This process is slow (more than 20 min), suggesting that surface and near subsurface oxygen vacancies could be involved. These results highlight the importance of the oxygen vacancies in the NO*x* adsorption/storage process on the YSZ surface. These punctual defects are able to transform and stabilize the interaction of NO_2 with the surface oxide without the presence of a conventional storage component such as BaO or alkaline cation. This catalyst feature is expected to further increase the material resistance to sulfur aging in NO*x*-trap application.

3.2.2. NOx storage capacity of Pt/YSZ

In order to evaluate the NO*x* storage capacity of the Pt/YSZ catalyst, the NO adsorption in the presence of oxygen was investigated under similar temperature and flow conditions to that described in Section 3.2.1. The variation of NO*x*, NO and NO_2 outlet concentrations as a function of time is presented in Fig. 7a. The small amount of NO_2 present in the inlet feed (~28 ppm) is produced via NO oxidation in the stainless steel pipes upstream

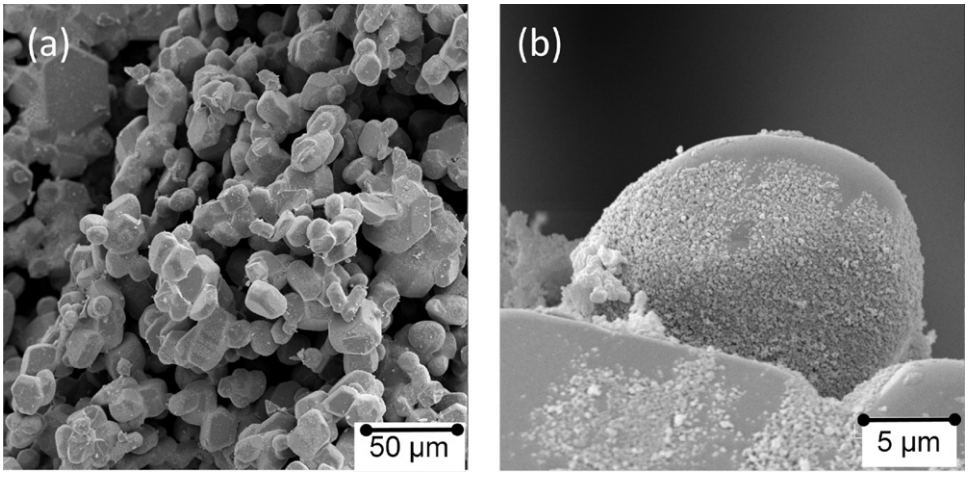

Fig. 5. SEM pictures of Pt/Rh/YSZ washcoat deposited inside a DPF porous wall (a) and on the surface of a SiC grain (b).

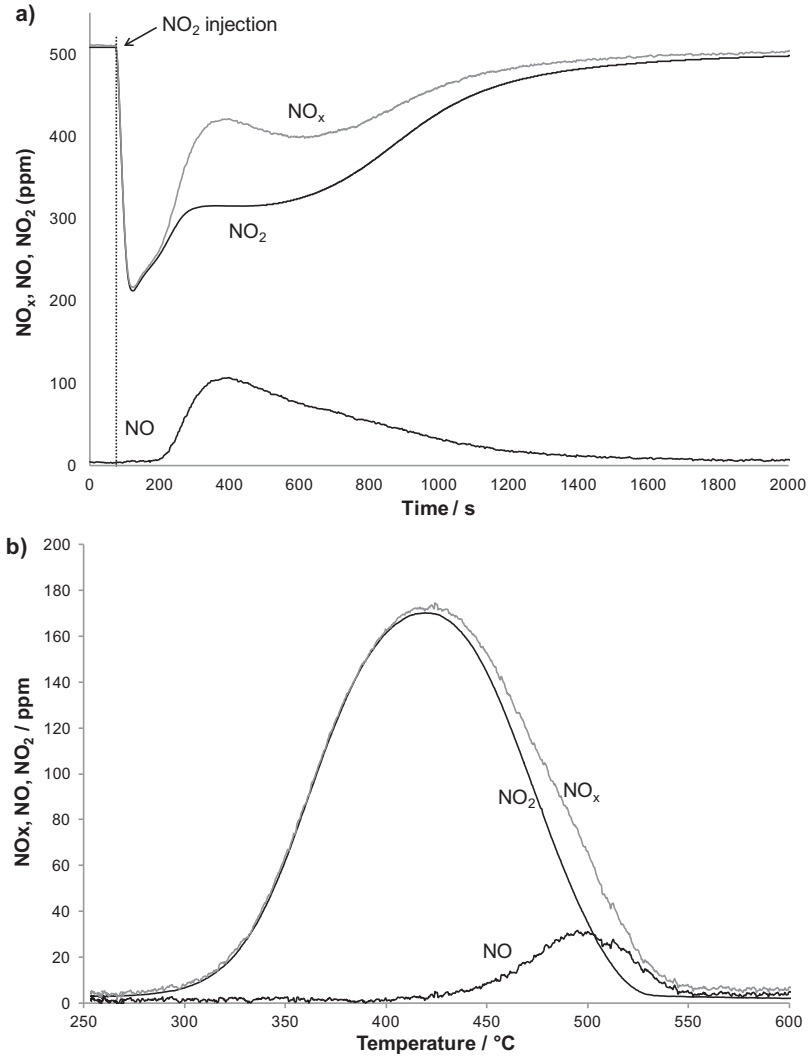

Fig. 6. Variations of NO*x*, NO and NO_2 concentrations as a function of time at 250 °C during the storage (a) and the desorption (b) on YSZ. Storage reactive mixture: NO_2/He: 500 ppm/He (10 L h^{-1}). Desorption conditions: He, flow = 10 L h^{-1}, heating ramp = 10 °C min^{-1}.

the reactor. NO and NO_2 inlet concentrations start to decrease when the feed comes into contact with the catalytic bed. NO concentration reaches a minimum value of 50 ppm while full NO_2 adsorption is sustained during above 60 s. After approximately 100 s, NO_2 emission starts to increase; the enhancement in the NO outlet concentration takes place nearly 75 s later. No production of NO is observed. After 700 s, the NO*x* storage process stops. Both NO and NO_2 concentrations reach a steady state which corresponds to the catalytic activity of Pt/YSZ for the NO oxidation reaction. Indeed, platinum-supported catalysts have been widely reported in the literature to be active in the NO to NO_2 oxidation reaction in presence of gaseous oxygen [27,28]. In the case of Ba-based NO*x*-trap systems, this reaction constitutes the rate-limiting step of the global NO*x* storage process. Indeed, NO_2 is rapidly adsorbed by the storage components on the catalyst surface, being in general stabilized as nitrate and/or nitrite species [29–31]. The total amount of NO*x* stored during this period of time is 34 μmol/g_{cat} (Table 2). We assume that NO_2 produced by the NO oxidation is stored on the catalyst until saturation of the surface. NO_2 storage is linked to nitrates, nitrites and/or oxy-nitrates formation onto Zr^{4+} cations after prior chemisorption on oxygen vacancies present on the YSZ surface support. No over-production of NO is observed most probably because the YSZ oxygen vacancies are quickly filled by gaseous oxygen, then inhibiting NO_2 disproportionation which requires three neighboring chemisorbed NO_2 molecules.

Desorption of the stored species in He as a function of temperature was performed up to 500 °C (Fig. 7b). As observed on YSZ material, two desorption peaks of NO_2 and NO take place at 334 and 380 °C, respectively. Both peaks are distinctly shifted toward lower temperatures in comparison with those recorded on the YSZ support (Fig. 6b), indicating that Pt promotes the NO_2 desorption from the vacancies as well as the nitrates decomposition. The corresponding amounts of NO_2 and NO released during the TPD process are 13 and 18 μmol/g_{cat} (31 μmol/g_{cat} of NO*x*), respectively (Table 2). These values are in good agreement with the total amount of NO*x* previously stored (34 μmol/g_{cat}). The total amount of NO*x* adsorbed on Pt/YSZ catalyst is smaller than that observed on YSZ support (48 μmol/g_{cat}) and the two components of the storage present opposite trends. The quantity of estimated from the NO_2 desorption peak, strongly decreases from 44 μmol/g_{cat} on YSZ down to 13 μmol/g_{cat} on Pt/YSZ. In addition, the NO desorption peak becomes predominant and clearly indicates that at least two different compounds were formed during the storage phases. This can be easily explained by the presence of oxygen in the gas phase during experiments on Pt/YSZ which modifies the nature of the stored NO*x* species as observed on Pt/Al_2O_3 [32]. Regarding

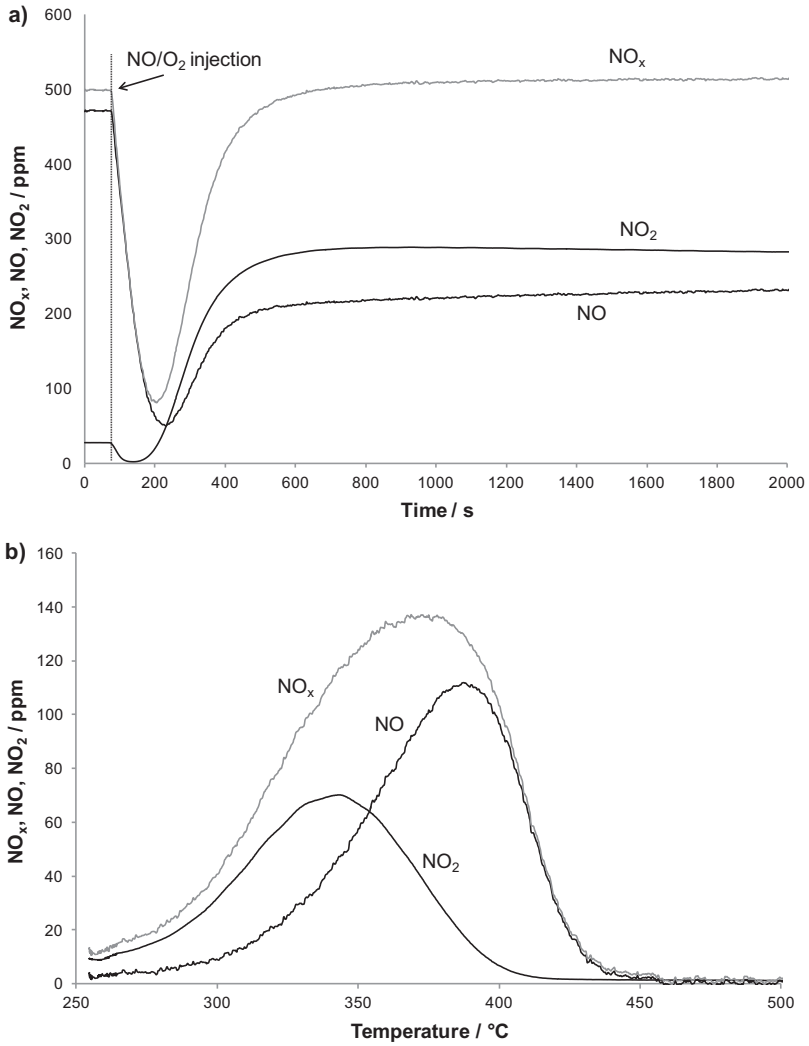

Fig. 7. Variations of NO*x*, NO and NO_2 concentrations as a function of time at 250 °C during the storage (a) and the desorption (b) on Pt/YSZ. Storage reactive mixture: NO/O_2/He: 500 ppm/6.7%. Overall flow: 10 L h^{-1}. Desorption conditions: He, flow = 10 L h^{-1}, heating ramp = 10 °C min^{-1}.

the drop of the NO*x* storage, this could be explained considering two main facts: (i) strong metal-support interactions through the surface oxygen vacancies have been described to be energetically favorable in nanoparticle-supported catalysts [33]. In this case, the presence of Pt on the YSZ surface can block the accessibility of the oxygen vacancies to the NO*x* species, due to preferential interactions of these punctual defects with Pt nanoparticles. (ii) in addition, participation of the oxygen vacancies in the O_2 activation, which constitutes a relevant step for NO oxidation on supported Pt clusters [34], is in competition with NO_2 chemisorption. Nevertheless, a remarkable NO*x* storage capacity can be obtained on the Pt/YSZ catalyst, by combining nitrates formation and NO_2 adsorption on oxygen vacancies. Therefore, the feasibility to use this kind of materials in the design of more efficient and stable NO*x* storage/reduction catalysts seems to be a promising alternative to the traditional systems (Ba-containing catalysts) employed for such application.

3.3. Catalytic activity measurements

The catalytic activity of Pt/Rh-YSZ supported catalysts was evaluated in the NO*x* storage/reduction (NSR) reaction under cyclic operation conditions. Rh nanoparticles were added in the catalyst formulation since it is well known that Rh strongly improves the regeneration efficiency [35].

3.3.1. NSR cycling process on Pt-Rh catalyst

Fig. 8 depicts the evolutions of NO*x* in the outlet feed as a function of time during the first five lean/rich cycles, performed at 200, 250 and 300 °C. During the lean phases, the profiles can be divided in three different zones, as already described by Epling et al. [16,36] on $Pt/Ba/Al_2O_3$ catalysts. First, complete or almost complete NO*x* uptake takes place. Then, NO*x* trapping rate decreases with a concomitant increase of the NO*x* concentration. At the last stage of adsorption, the NO*x* concentration reaches a steady state, indicating the saturation of the catalyst surface. This steady state is lower than the inlet NO*x* concentration because selective catalytic reduction (SCR) of NO*x* by C_3H_6 occurs on Pt [36] even after the surface saturation. During the rich phase, decomposition and subsequent reduction of stored species take place over the noble metal sites. This process is characterized by a fast decay of NO*x* outlet concentration.

For Pt-Rh catalyst, NO*x* profiles obtained during the lean and rich phases (LP and RP) are different depending on the temperature reaction. At 200 °C, the trapping rate of NO*x* decreases (higher slope) with increasing cycle number. SCR NO*x* conversions were

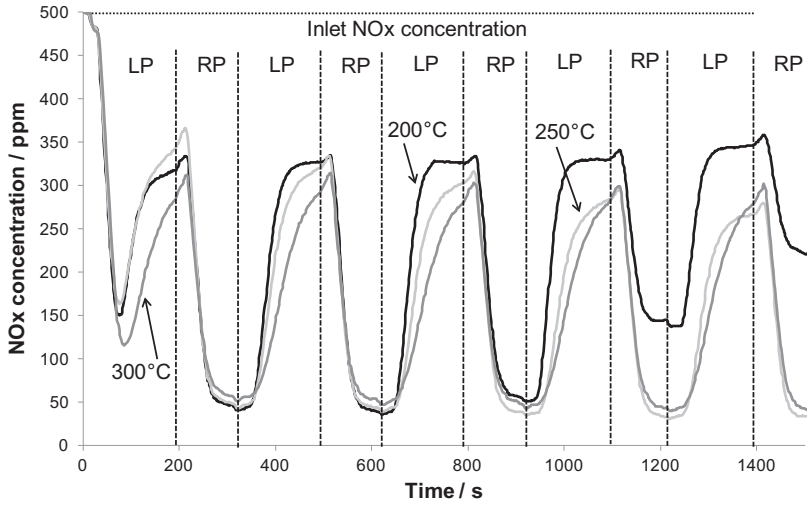

Fig. 8. Variation of the NO*x* concentration versus time during LP/RP cycles on Pt/Rh/YSZ. Lean phase (LP): NO*x* (500 ppm); C_3H_6 (500 ppm); O_2 (6.5%); H_2O (10%), 3 min. Rich phase (RP): NO*x* (500 ppm); C_3H_6 (500 ppm), 2 min. Overall flow: 10 L h^{-1}.

estimated from the steady state NO*x* concentration value at the end of the lean phase. At 200 °C, the SCR NO*x* conversion decreases with time starting at 37% during the first cycle down to less than 18% after the seventh. On the other hand, at 250 °C, we observe a slight activation of the catalyst with a SCR NO*x* conversion of 32% during the first cycle which increases to a constant value of 47% after 5 cycles. The SCR NO*x* conversion at 300 °C is quite stable at 47%. Whatever the temperature, we observe a small peak of NO*x* desorption at the beginning of the rich phases. During a few seconds, the NO*x* release rate is higher than the NO*x* catalytic reduction process. At 200 °C, the catalyst regeneration seems to be impaired after the third cycle, while at 250 and 300 °C the NO*x* profiles remain reproducible cycle by cycle. This result confirms that, at 200 °C, the NO*x* storage capacity and catalytic properties rapidly decrease, suggesting a catalyst deactivation.

Table 3 summarizes the performances of the Pt-Rh catalyst at 250 and 300 °C. Overall NO*x* abatement is fairly similar at 250 °C and 300 °C and reaches 73–75%. On the other hand, the selectivity into N_2 strongly increases with temperature from 65% at 250 °C up to 88% at 300 °C. This is due to the production of N_2O during SCR of NO*x* by propene on Pt which decreases with temperature [37,38]. Similar experimental conditions (LP: 400 ppm NO, 400 ppm C_3H_6, 8% O_2, 5 min and RP: 400 ppm NO, 400 ppm C_3H_6, 5 min) were recently used to test the catalytic performances of bimetallic Pt and Rh dispersed on $BaCO_3/\gamma$-Al_2O_3 [39]. Catalysts were prepared with flame spray pyrolysis method. Best performances were achieved when Pt (0.5 wt%) was dispersed on γ-Al_2O_3 (167 m^2 g^{-1}) while Rh (0.5 wt%) was deposited on $BaCO_3$. Without the presence of SO_2 in the gas phase, NO*x* conversion reached, at 300 °C, values of 57% and 80% for a space velocity of 300,000 h^{-1} and 38,000 h^{-1}, respectively. Using shorter phases (LP: 500 ppm NO, 10% O_2, 0.13% CO—H_2 (75%/25%), 1% CO_2, 167 ppm C_3H_6, 100 s and RP: 500 ppm NO, 8.53% CO—H_2, 1% CO_2, 10 s), Corbos et al. [40] have investigated the coupling of a Pt (1 wt%)-Rh (0.013 wt%)/Ba (20 wt%)/Al_2O_3 (190 m^2 g^{-1}) catalyst with Cu/ZSM-5, a NH_3-SCR material. For a space velocity of 55,000 h^{-1}, the NO*x* conversion achieved 86% and 79% at 250 °C and 300 °C, respectively. All these performances obtained with optimized or promoted Ba-reference NSR catalysts are comparable with those of the Pt-Rh catalyst which exhibits a NO*x* conversion of 75% at 300 °C for a space velocity of 100,000 h^{-1}. This confirms that YSZ can be used as a NO*x* storage material in cycling conditions.

Table 3
Catalytic performances of the catalysts.

Catalysts	NO*x* conversion during a complete cycle (9th cycle)/%		N_2 selectivity during a complete cycle (9th cycle)/%	
	250 °C	300 °C	250 °C	300 °C
Pt-Rh	73	75	65	88
Fresh Pt-Rh/DPF	66	55	68	82
Aged Pt-Rh/DPF	46	55	72	82

3.3.2. NSR cycling process on Pt-Rh/DPF catalyst

Catalytic performances of the Pt/Rh DPF catalysts were investigated by using shorter phases (1 min for the lean phase and 30 s for the rich phase) and higher flow (40 L h^{-1}). Variations of the NO*x* concentration during ten successive cycles at 200 °C, 250 °C and 300 °C are plotted in Figure 9a. As already observed on powdered Pt-Rh catalyst, the NO*x* conversion drops with increasing cycle number at 200 °C. This is probably due to a slow regeneration process during the rich phases. In addition, Figure 9b shows that the CO_2 production during the initial lean phase is low compared to that recorded at 250 °C and 300 °C, demonstrating that at 200 °C, the catalytic activity is not sufficient to fully oxidize propene. At 250 °C and 300 °C, quite reproducible cycles are achieved after 200 s. NO*x* conversions reach 66% and 55% at 250 °C and 300 °C, respectively. Unfortunately, we observed significant production of N_2O at 250 °C (around 60 ppm) at the lean/rich transition. Therefore, the NO*x* conversion into N_2 is found to be equivalent at 250 °C and 300 °C, around 45% (Fig. 10). CO_2 production during cycles, exposed in Fig. 9b, confirms that the catalytic activity is low at 200 °C. Propene is not fully oxidized during lean phases at 200 °C. On the opposite, CO_2 production at 250 and 300 °C during lean phases corresponds to full propene conversion. A sharp peak of CO_2 emission is observed at the beginning of each lean phase. This is due to the oxidation of carbon deposited during the previous rich phase. Indeed, the Boudouard reaction (3) can occur in this temperature range, while CO is produced via steam reforming of propene (4).

$$2CO \rightarrow C(s) + CO_2(g) \quad (3)$$

$$C_3H_6 + 3H_2O \rightarrow 3CO + 6H_2 \quad (4)$$

During rich phases, we observe high concentrations of CO_2 which are partially due to the Boudouard reaction. We have estimated the quantity of carbon deposition from the sharp CO_2 peak

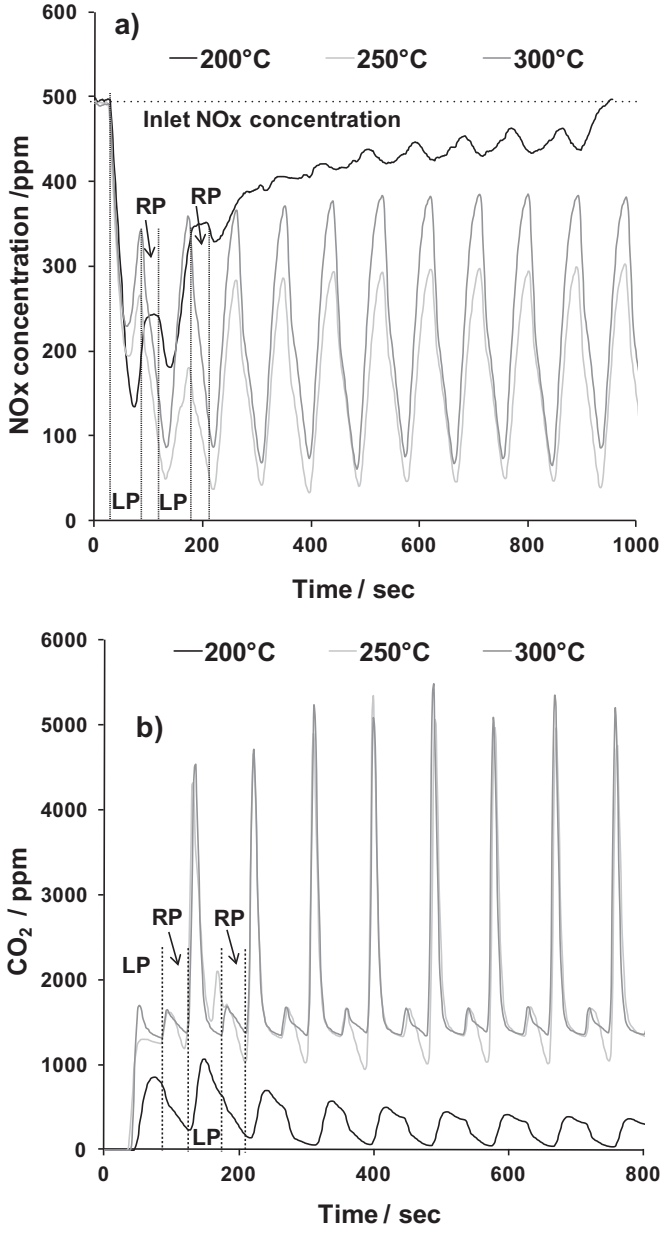

Fig. 9. Variations of NO*x* (a) and CO_2 (b) concentrations during lean/rich cycles at 200 °C, 250 °C and 300 °C on Pt-Rh/DPF. Lean/Rich cycle: 1 min/0.5 min. Overall flow: 40 L h^{-1}.

at the beginning of the lean phase and found that this cannot explain the high CO_2 overproduction recorded during rich phases. We assume that this CO_2 overproduction is due to electrochemical oxidation of CO by O^{2-} ions contained in the YSZ support. Fig. 10 displays values of NO*x* conversion into N_2 after aging the Pt-Rh/DPF monolith at 700 °C for 10 h in air containing 10 vol.% H_2O following by an exposure at 300 °C for 6 h to a mixture containing 10 vol.% H_2O and 100 ppm SO_2. At 250 °C, we observe a decrease of the conversion from 45% to 35% while no significant deactivation is recorded at higher temperatures. Production of CO_2 during lean cycles at 250 °C shows that propene is not fully oxidized. This indicates that the catalytic activity drop observed at 250 °C is due to metallic nanoparticles sintering which leads to a decrease of metallic active surface availability. On the other hand, quite reproducible and stable NO*x* conversions are achieved. These results underline the excellent sulfur tolerance of the Pt-Rh/DPF sample.

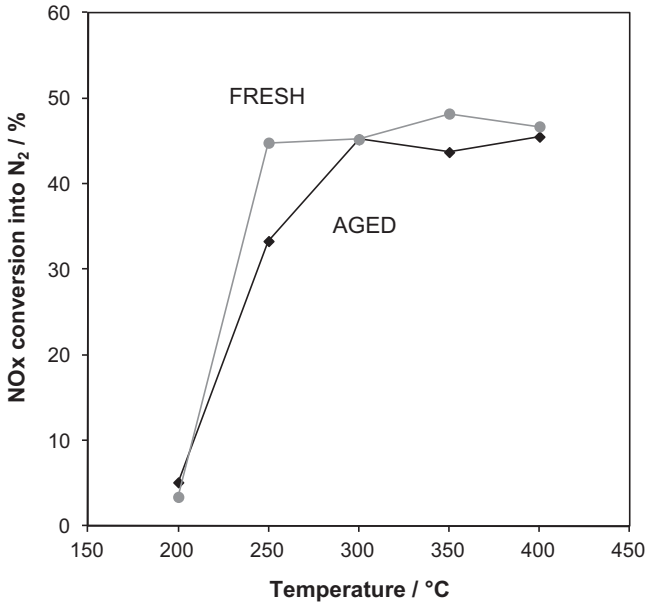

Fig. 10. NO*x* conversion into N_2 as a function of the temperature for fresh and aged Pt-Rh/DPF. Aging procedure: calcinations at 700 °C for 10 h in air containing 10 vol.% H_2O and at 300 °C for 6 h in air containing 10 vol.% H_2O and 100 ppm SO_2.

4. Conclusions

Yttria-stabilized zirconia (YSZ) was used as a support of NSR catalysts. A remarkable NO*x* storage capacity was obtained on Pt/YSZ powdered catalysts, by combining nitrates formation and NO_2 adsorption on oxygen vacancies. Under cycling conditions, powdered Pt-Rh catalyst exhibited overall NO*x* abatement conversion around 75% at 250 and 300 °C. Pt/Rh/YSZ catalysts were deposited in the porosity of SiC mini diesel particulate filters (DPFs). The YSZ-based washcoat was formed of nanometric ceramic grains which homogeneously cover SiC grains surface both in the channels and inside the walls. Pt and Rh nanoparticles (1–3 nm) were found to be highly dispersed. Quite reproducible and stable NO*x* conversions were achieved in cycling conditions with values of around 50% between 250 and 400 °C. In addition, YSZ-based NSR catalysts have shown high thermal resistance and sulfur tolerance.

Acknowledgement

The authors would like to thank the staff of the microscopy service of IRCELYON for SEM and TEM analysis.

References

[1] N. Takahashi, H. Shinjoh, T. Iijima, T. Suzuki, K. Yamazaki, K. Yokota, H. Suzuki, N. Miyoshi, S. Matsumoto, T. Tanizawa, T. Tanaka, S. Tateishi, K. Kasahara, Catalysis Today 27 (1996) 63–69.
[2] S. Roy, A. Baiker, Chemical Reviews 109 (2009) 4054–4091.
[3] P. Granger, V.I. Parvulescu, Chemical Reviews 111 (2011) 3155–3207.
[4] J. Suzuki, S. Matsumoto, Topics in Catalysis 28 (2004) 171–176.
[5] J.E. Kirwan, M. Shost, G. Roth, J. Zizelman, SAE International Journal of Engines 3 (1) (2010) 355–371.
[6] K.S. Martirosyan, K. Chen, D. Luss, Chemical Engineering Science 65 (2010) 42–46.
[7] K. Chen, K.S. Martirosyan, D. Luss, Chemical Engineering Journal 176–177 (2011) 144–150.
[8] A. Hadjar, W.Y. Hernandez, A. Princivalle, C. Tardivat, C. Guizard, P. Vernoux, Electrochemistry Communications 13 (2011) 924–927.
[9] G. Blanchard, S. Rousseau, L. Mazri, L. Lizarraga, A. Giroir-Fendler, B. D'Anna, P. Vernoux, Patent No. WO 2011098718 (A1).
[10] M. Alves Fortunato, D. Aubert, C. Capdeillayre, C. Daniel, A. Hadjar, A. Princivallea, C. Guizard, P. Vernoux, Applied Catalysis A 403 (2011) 18–24.
[11] M. Boudart, G. Djega-Mariadassou, Handbook of Heterogeneous Catalytic Reactions, Princeton University Press, NY, 1984.

[12] T. Vergunst, F. Kapteijn, J.A. Moulijn, Applied Catalysis A 213 (2001) 179–187.
[13] L. Villegas, F. Masset, N. Guilhaume, Applied Catalysis A 320 (2007) 43–55.
[14] Y. Zhang, C.Y. Zhao, H. Liang, Y. Liu, Catalysis Letters 127 (2009) 339–347.
[15] L. Olsson, H. Persson, E. Fridell, M. Skoglundh, B. Andersson, Journal of Physical Chemistry B 105 (2001) 6895–6906.
[16] W.S. Epling, J.E. Parks, G.C. Campbell, A. Yezerets, N.W. Currier, L.E. Campbell, Catalysis Today 96 (2004) 21–30.
[17] A. Lindholm, N.W. Currier, J.L. Li, A. Yezerets, L. Olsson, Catalysis Journal 258 (2008) 273–288.
[18] J.A. Rodriguez, T. Jirsak, G. Liu, J. Hrbek, J. Dvorak, A. Maiti, Journal of the American Chemical Society 123 (2001) 9597–9605.
[19] G. Liu, J.A. Rodriguez, J. Hrbek, J. Dvorak, C.H.F. Peden, Journal of Physical Chemistry B 105 (2001) 7762–7770.
[20] M. Daturi, N. Bion, J. Saussey, J.-C. Lavalley, C. Hedouin, T. Seguelong, G. Blanchard, Physical Chemistry Chemical Physics 3 (2001) 252–255.
[21] S. Kikuyama, I. Matsukuma, R. Kikuchi, K. Sasaki, K. Eguchi, Applied Catalysis A 226 (2002) 23–30.
[22] I. Matsukuma, S. Kikuyama, R. Kikuchi, K. Sasaki, K. Eguchi, Applied Catalysis B 37 (2002) 107–115.
[23] H. Miyata, S. Konishi, T. Ohno, F. Hatayama, J. Chem Soc, Faraday Transactions 91 (1995) 1557–1562.
[24] R.G. Silver, C.J. Hou, J.G. Ekerdt, Journal of Catalysis 118 (1989) 400–416.
[25] W.J. Fleming, Journal of the Electrochemical Society 124 (1977) 21–28.
[26] W.P. Dow, Y.P. Wang, T.J. Huang, Journal of Catalysis 160 (1996) 155–170.
[27] S. Benard, L. Retailleau, F. Gaillard, P. Vernoux, A. Giroir-Fendler, Applied Catalysis B 55 (2005) 11–21.
[28] P.J. Schmitz, R.J. Kudla, A.R. Drews, A.E. Chen, C.K. Lowe-Ma, R.W. McCabe, W.F. Schneider, C.T. Goralski Jr., Applied Catalysis B 67 (2006) 246–256.
[29] X. Li, P. Vernoux, Applied Catalysis B 61 (2005) 267–273.
[30] S. Hodjati, P. Bernhardt, C. Petit, V. Pitchon, A. Kiennemann, Applied Catalysis B 19 (1998) 209–219.
[31] S. Hodjati, P. Bernhardt, C. Petit, V. Pitchon, A. Kiennemann, Applied Catalysis B 19 (1998) 221–232.
[32] F. Prinetto, G. Ghiotti, I. Nova, L. Lietti, E. Tronconi, P. Forzatti, Journal of Physical Chemistry B 105 (2001) 12732–12745.
[33] M.G. Sanchez, J.L. Gazquez, Journal of Catalysis 104 (1987) 120–135.
[34] B.M. Weiss, E. Iglesia, Journal of Physical Chemistry C 113 (2009) 13331–13340.
[35] A. Amberntsson, E. Fridell, M. Skoglundh, Applied Catalysis A 46 (2003) 429–439.
[36] W.S. Epling, A. Yezerets, N.W. Currier, Applied Catalysis B 74 (2007) 117–129.
[37] A. Obuchi, A. Ohi, M. Nakamura, A. Ogata, K. Mizuno, H. Ohuchi, Applied Catalysis B 2 (1993) 71–80.
[38] R. Burch, P.J. Millington, Catalysis Today 26 (1995) 185–206.
[39] R. Büchel, S.E. Pratsinis, A. Baiker, Applied Catalysis B 113–114 (2012) 160–171.
[40] E.C. Corbos, M. Haneda, X. Courtois, P. Marecot, D. Duprez, H. Hamada, Applied Catalysis A 365 (2009) 187–193.